Article

Journal of the Brazilian Chemical Society

https://dx.doi.org/10.21577/0103-5053.20240108

J. Braz. Chem. Soc. **2025**, *36*, 1, e-20240108, 1-14
©2025 Sociedade Brasileira de Química

Investigating the Inhibitory Mechanism of *para*-Sulfonato-calix[4]arenes against Polymerase and Helicase of SARS-CoV-2: Molecular Docking and Dynamics Simulation Studies

Khalid Khan, [a] ***Habib Rahman,*** [a] ***Tanzeel Shah,*** [b] ***Haroon ur Rashid,*** [c] ***Nasir Ahmad,*** [a] ***Akhtar Muhammad,*** [a] ***Muhammad Naveed Umar,*** [d] ***Naila Gulfam,*** [e] ***Muhammad Zahoor,*** [f] ***Riaz Ullah*** [g] ***and Essam A. Ali*** [h]

[a]*Department of Chemistry, Islamia College University, Peshawar, 25120, KP, Pakistan*

[b]*Institute of Basic Medical Sciences, Khyber Medical University, Peshawar, 25120, KP, Pakistan*

[c]*Centro de Ciências Químicas, Farmacêuticas e de Alimentos, Universidade Federal de Pelotas, 96010-900 Pelotas-RS, Brazil*

[d]*Department of Chemistry, University of Liverpool, Liverpool, L3 5TR, United Kingdom*

[e]*Department of Zoology, Jinnah College for Women, University of Peshawar, Peshawar, 25120, KP, Pakistan*

[f]*Department of Biochemistry, University of Malakand, Chakdara Dir Lower, 18800, KP, Pakistan*

[g]*Department of Pharmacognosy, College of Pharmacy, King Saud University, Riyadh 11451, Saudi Arabia*

[h]*Department of Pharmaceutical Chemistry, College of Pharmacy King Saud University Riyadh, 11451, Saudi Arabia*

The coronavirus disease (COVID-19) pandemic, caused by the severe acute respiratory syndrome coronavirus 2 (SARS-CoV-2), has had a profound impact on global health and socio-economic conditions. To date, various vaccines have been administered worldwide in an effort to curb the spread of the virus. Despite vaccination efforts, there have been complications. Existing antiviral drugs have shown limited effectiveness, prompting the use of computational methods to understand the dynamics of the virus and develop suitable treatments. The current study focuses on using biocompatible *para*-sulfonato-calix[4]arenes to dock against two key proteins of SARS-CoV-2, namely ribonucleic acid (RNA)-dependent RNA polymerase, and helicase. Docking results indicate a strong binding affinity of these compounds to the target proteins, with higher scores compared to commonly used medications. Molecular dynamics (MD) simulation validates the docking results, showing stable protein-ligand complexes over time. The compounds are also screened for absorption, distribution, metabolism, and excretion properties and toxicity, suggesting their potential as lead candidates for inhibiting the virus's key proteins. However, further *in vivo* and *in vitro* studies are recommended to confirm these findings.

Keywords: coronavirus, helicase, *para*-sulfonato-calix[4]arenes, molecular docking, MD simulations

Introduction

A novel coronavirus emerged in Wuhan City, China, in December 2019.[1,2] This new virus, responsible for severe respiratory syndrome, quickly spread globally. Consequently, the World Health Organization (WHO) declared a Public Health Emergency of International Concern on January 30, 2020.[3,4] As of WHO's report in 2024,[5] the deadly severe acute respiratory syndrome coronavirus 2 (SARS-CoV-2) has infected 0.776 billion people worldwide and caused 7.1 million deaths. Moreover, it has had a significant adverse impact on the global economy. SARS-CoV-2 belongs to the Coronaviridae family and β-coronavirus genus. Other viruses within this genus, such as severe acute respiratory syndrome coronavirus (SARS-CoV), Middle East respiratory syndrome coronavirus (MERS-CoV), human coronavirus OC43 (HCoV-OC43), and human coronavirus HKU1 (HCoV-HKU1), can also infect humans.[6-8] The SARS-CoV-2 genome consists of a positive-sense single stranded RNA with a size varies

*e-mail: drkhalidchem@yahoo.com, mohammadzahoorus@yahoo.com
Editor handled this article: Paula Homem-de-Mello (Associate)

This is an open-access article distributed under the terms of the Creative Commons Attribution License.

from 29.8 kb to 29.9 kb and contains 14 open reading frames (ORFs). These ORFs are responsible for encoding 27 structural and non-structural proteins. At the 5'-end of the genome, ORF-1a and ORF-1ab encode information for two lengthy polypeptide segments, pp1a, and pp1ab. These two polyproteins further provide information for the synthesis of 15 non-structural proteins (nsp1-10 and nsp12-16). Notable non-structural proteins include nsp3 (a multi-domain protein with the PL-pro domain), nsp5 (3CL chymotrypsin-like), nsp9 (a helicase involved in viral replication), nsp12 RNA-dependent RNA polymerase (RdRp), and nsp13 (helicase). Conversely, at the 3' end of the genome, details about the four structural and eight auxiliary proteins are provided. The accessory proteins are 3a, 3b, p6, 7a, 7b, 8b, 9b, and orf14; the structural proteins comprise spike surface glycoproteins (S), envelope (E), matrix (M), and nucleocapsid (N) proteins.[7] On one hand, the structural proteins of coronaviruses, such as spike (S) proteins, display a high degree of variability, making them unsuitable targets for drug design. On the other hand, non-structural proteins such as helicase (nsp13) and RNA-dependent RNA polymerase (nsp12) are conserved proteins and are considered prime targets for viral inhibition. The viral life cycle relies heavily on RdRp, which is crucial for RNA genome replication and transcription. Furthermore, RdRp is seen as an attractive target in drug discovery and development because it lacks a homolog in mammalian cells, and inhibiting it is not expected to result in target-related side effects.[9] During biological processes such as recombination, replication, and repair, the helicase enzyme facilitates the unwinding of double-stranded nucleic acids in the 5' to 3' direction. Because of their highly conserved genomic sequences, unique functions, and distinctive active sites, the RNA-dependent RNA polymerase (nsp12) and helicase (nsp13) of SARS-CoV-2 were selected as target proteins in this study.[10] Research is underway in two main areas to combat the disease: designing, developing, and formulating antiviral drugs, and developing vaccines. Numerous vaccines have been developed and applied, yielding diverse results.[11] Similarly, several antiviral drugs, such as favipiravir, chloroquine, oseltamivir, hydroxychloroquine, and ribavirin, among others, have been utilized, with some drugs currently undergoing clinical trials.[12,13] Phytocompounds from various medicinal plants have also been investigated using *in silico* models.[14,15] The results of these studies have not been satisfactory, suggesting the need for further research to design, develop, and formulate more selective and potent drugs for the effective treatment of coronavirus disease (COVID-19). Consequently, in this study, *para*-sulfonato-calix[*n*]arenes were chosen as promising drug candidates for inhibiting the RdRp and helicase enzymes of SARS-CoV-2. This selection was based on their notable features, including ease of synthesis in significant quantities, high water solubility, various complexation driving forces such as hydrophobic, π-π stacking, π-alkyl, π-sulfur, and hydrogen bond interactions, framework rigidity, biocompatibility, and robust binding ability of the upper rim sulfonate groups. Furthermore, toxicity studies indicate that *para*-sulfonato-calix[*n*]arenes can be safely utilized with a single injected dose equivalent to 2-5 g in humans.[16,17] In addition to the aforementioned features, *para*-sulfonato-calix[*n*]arenes have also demonstrated antiviral activity against human coronavirus 229E,[18] providing a strong rationale for investigating their antiviral activity against SARS-CoV-2. Consequently, this study was conducted to target the active sites of two crucial enzymes, namely RdRp, and helicase of SARS-CoV-2, using biocompatible molecules of *para*-sulfonato-calix[*n*]arenes through computational approaches.

Methodology

Proteins and selected compounds preparation

Crystal structures of the RdRp (PDB ID: 7C2K) and helicase (PDB ID: 6ZSL) with resolutions of 2.93 and 1.94 Å, respectively, were retrieved from the Protein Data Bank website.[19] The selected proteins were prepared using Discovery Studio,[20] involving several processes such as the removal of heteroatoms, addition of hydrogen atoms, and selection of active sites. Subsequently, the target structures were converted to pdbqt format using PyRx[21] which automatically removes solvent molecules, followed by energy minimization and calculation of Gasteiger charges.[22] Similarly, *para*-sulfonato-calix[4]arenes (**L1-L4**), their open-chain analog (**L6**), and calix[4]arene (**L5**) were drawn using ChemDraw, software[23] and saved in mol format. These structures were then converted to PDB format using Open Babel.[24] Before molecular docking analysis, they underwent an energy minimization process using the MMFF94 forcefield technique and were subsequently converted into PDBQT format using the Open Babel tool in PyRx.[20] The chemical structures of *para*-sulfonato-calix[4]arenes (**L1-L6**) are depicted in Figure 1.

Molecular docking analysis

The selected ligands (**L1-L6**) were docked against the prepared structures of target proteins using AutoDock Vina[25] integrated into PyRx software. AutoDock Vina was chosen

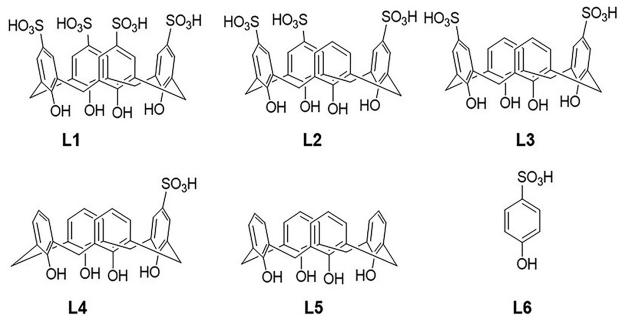

Figure 1. Structures of *para*-sulfonato-calix[4]arenes (**L1-L4**), calix[4]arene (**L5**) and open chain analogue (**L6**) of *para*-sulfonato-calix[4]arenes. **L1**: 25,26,27,28-tetrahydroxycalix[4]arene-5,11,17,23-tetrasulfonic acid, **L2**: 25,26,27,28-tetrahydroxycalix[4]arene-5,11,17-trisulfonic acid, **L3**: 25,26,27,28-tetrahydroxycalix[4]arene-5,17-disulfonic acid, **L4**: 25,26,27,28-tetrahydroxycalix[4]arene-5-sulfonic acid, **L5**: calix[4]arene-25,26,27,28-tetrol and **L6**: 4-hydroxybenzenesulfonic acid.

for docking due to its enhanced speed and accuracy. The bonds of the selected ligands were allowed to be rotatable during the docking process. The Lamarckian Genetic Algorithm (LGA) approach was utilized for all calculations, enabling protein-fixed and ligand-flexible docking.[26] During the docking process, the number of binding modes and the exhaustiveness value for both macromolecules were set to 8. For RdRp, the grid box size was set to 74.81 Å × 84.54 Å × 85.72 Å with the grid center at coordinates (120.05, 123.86, 120.15 Å) for x, y, and z axes, respectively. For helicase, the grid box size was fixed at 51.37 Å × 66.97 Å × 59.61 Å with the grid center at coordinates (26.28, 12.60, 58.96 Å) for x, y, and z axes, respectively. Using Discovery Studio Visualizer,[20] non-covalent interactions of protein-ligand complexes such as hydrogen bonds and bond lengths were examined.[27]

Molecular dynamics simulation assay

Molecular dynamics (MD) simulations of the protein-ligand complexes were conducted using the Linux 5.4 package[28] and GROMACS 2021.1 version.[29] The ligand topologies were generated using the CGenFF service,[30] while the CHARMM36 force field was employed for the proteins.[31] Simple point charge (SPC) water model was employed to solvate all the complexes within a rectangular box. The simulation system was neutralized by adding the necessary quantity of Na^+ and Cl^- ions, achieving an electrically neutral state. The salt concentration in each system was set at 0.15 mol L^{-1} (corresponding to physiological conditions of 0.15 M NaCl). Subsequently, all solvated systems underwent energy minimization for 5,000 steps using the steepest descent method. Following this, MD simulation was conducted, including NVT (constant number of particles, volume, and temperature) and NPT (constant number of particles, pressure, and temperature) series. Both series were carried out for a total of 300 ps at a temperature of 300 K and a pressure of 1 atm. The V-rescale thermostat and the Parrinello-Rahman barostat were selected for temperature and pressure control, respectively. Subsequently, a production run was executed for 100 ns at 300 K temperature and 1 atm pressure. The stability of protein-ligand complexes was assessed through comparative analyses of root mean square fluctuation (RMSF), root mean square deviation (RMSD), radius of gyration (Rg), principal component analysis (PCA), solvent-accessible surface area (SASA), and hydrogen bonds. Plots of the data were generated using the XMGRACE software.[32]

MM/PBSA binding free energy calculation

To gain a comprehensive understanding of the molecular interactions between the target proteins and selected compounds, the MM/PBSA (Molecular Mechanics/Poisson Boltzmann Surface Area) binding free energies were calculated using the g_mmpbsa package within GROMACS27. These calculations were performed using the last 20 ns of the MD production run, sampled at intervals of 100 ps. The production run was conducted at a temperature of 300 K and a pressure of 1 atm for all intervals. The free solvation energy (comprising polar and nonpolar solvation energies) and potential energy (including electrostatic and van der Waals interactions) of each protein-compound complex were analyzed to assess the overall ΔG binding.[33,34] The binding energies were calculated using the following equation:

$$\Delta G_b = G_c - (G_p + G_l) \quad (1)$$

where, ΔG_b: total binding energy of the protein-**L1** complex, G_p: binding energy of free protein, G_C: free energy of complex, and G_l: binding energy of unbound compound **L1**.

Prediction of ADME and toxicity

The Absorption, Distribution, Metabolism, and Excretion (ADME) and toxicity properties of compounds (**L1-L6**) were studied. Pharmacokinetics and pharmacodynamics properties such as lipophilicity (Log $P_{o/w}$), number of rotatable bonds, water solubility (Log S), blood-brain barrier (BBB) permeation, and Lipinski's rules.[35] were predicted using the SwissADME service.[36] Toxicity profiles, including hepatotoxicity, carcinogenicity, immunotoxicity, mutagenicity, cytotoxicity, ecotoxicity, clinical toxicity, median lethal dose 50 (LD_{50}), and toxicity class, were predicted using ProTox 3.0.[37]

Results

Docking analysis of selected compounds against RdRp

Selected compounds (**L1-L6**) were docked against the active sites of RdRp. Results reveal that compound **L1** developed seven physical interactions with the active site of the RdRp enzyme of SARS-CoV-2, resulting in the highest binding affinity and more negative binding energy of −8.9 kcal mol^{-1} among all screened compounds (Table 1). One sulfonate group of **L1** contributed significantly to the complex formation with RdRp by forming three conventional hydrogen bonds with three residues: Trp619, Trp802, and Ala764, respectively. Each of the residues, Asp620, and Tyr621 formed a single conventional hydrogen bond with the phenolic group of **L1**. Residue Asp762 generated a pi-anion interaction with the benzene ring of **L1**. Amino acid Arg557 was involved in a carbon-hydrogen interaction with the oxygen atom of another sulfonate group of **L1**. Results suggest that two sulfonate groups at the upper rim, two phenolic groups at the lower rim, and one benzene ring of **L1** are effectively involved in complex formation with the RdRp enzyme of SARS-CoV-2 (Figures 2 and S1, Supplementary Information (SI) section). Similarly, **L2** generated eleven non-covalent interactions with the RdRp macromolecule; these physical forces resulted in a binding energy of −8.7 kcal mol^{-1} (Table 1). Residue Arg838 was

Table 1. Binding affinity, number of interactions, nature of interactions, distance of interactions, and interacting residues of selected compounds (**L1-L6**) against RdRp

Compound	Binding energy / (kcal mol^{-1})	Number of interactions	Nature of interactions	Interaction distance / Å	Interacting residues
L1	−8.9	7	Pi-anion	4.32	Asp762
			H-bond	3.33	Trp619
			H-bond	2.98	Trp802
			H-bond	3.15	Asp620
			H-bond	3.08	Tyr621
			H-bond	3.43	Ala764
			Carbon-H	3.99	Arg557
L2	−8.7	11	Pi-sulfur	4.53	His441
			H-bond	2.49	Thr558
			H-bond	3.72	Asp454
			Pi-alkyl	4.52	Arg555
			Pi-sigma	3.98	Lys623
			H-bond	2.70	Lys547
			Carbon-H	4.79	Lys547
			H-bond	2.69	Ala552
			H-bond	3.78	Agr838
			H-bond	4.52	Agr838
			Carbon-H	5.24	Ser551
L3	−8.5	5	H-bond	2.51	Asp620
			Pi-alkyl	4.85	Lys623
			H-bond	2.87	Asp736
			H-bond	3.07	Ser816
			Carbon-H	4.16	Arg557
L4	−8.1	6	H-bond	2.60	Thr396
			Pi-alkyl	2.91	Pro325
			Pi-alkyl	5.51	Pro325
			Pi-alkyl	4.65	Pro697
			Pi-sigma	3.67	Phe398
			Carbon-H	4.04	Cys397
L5	−6.2	5	H-bond	2.30	Thr396
			Pi-alkyl	5.43	Pro325
			Pi-alkyl	3.79	Pro325
			Pi-alkyl	5.30	Pro697
			Pi-sigma	4.02	Phe398
L6	−5.3	5	Pi-anion	3.65	Asp625
			H-bond	3.01	Thr682
			H-bond	2.99	Ser684
			H-bond	3.40	Arg626
			H-bond	2.75	Tyr658

associated with two conventional hydrogen bonds with one sulfonate group of **L2**; it mainly contributes to the formation of the protein-**L2** complex. Each of the amino acids Lys547, Thr558, Ala552, and Asp454 formed a single hydrogen bond with three different sulfonate groups at the upper rim of **L2**. The residues Ser551 and Lys547 generated a single carbon-hydrogen interaction with two sulfonate groups of **L2**. In addition, some weak interactions such as pi-alkyl, pi-sulfur, and pi-sigma also occurred between residues Arg555, His441, and Lys623 of RdRp, and one sulfonate group and two benzene rings of **L2**, respectively (Figures 2 and S1). Compound **L3** developed five physical interactions with the target protein, generating a binding energy of –8.5 kcal mol^{-1} (Table 1). Each of the residues Asp736 and Ser816 formed a single conventional hydrogen bond with one sulfonate group; the residue Asp620 also formed a hydrogen bond with the phenolic group of **L3**. Residue Lys623 was involved in a pi-alkyl interaction with the benzene ring of **L3**, while residue Arg557 was associated with the sulfonate group of L3 through a carbon-hydrogen interaction (Figures 2 and S1). Similarly, **L4** resulted in six non-covalent interactions with the receptor protein; these forces led to a binding energy of –8.1 kcal mol^{-1} (Table 1).

Residue Thr396 formed one hydrogen bond with a phenolic group of **L4**. Amino acid Pro325 was involved in two pi-alkyl interactions with two benzene rings of **L4**; residue Pro697 contributed to a pi-alkyl interaction with another benzene ring of **L4**. Furthermore, Phe398 and Cys397 formed pi-sigma and carbon-hydrogen interactions with the benzene ring and phenolic group of **L4**, respectively (Figures 2 and S1).

Compound **L5** formed five physical interactions with the active sites of the RdRp enzyme, resulting in a binding energy of –6.2 kcal mol^{-1} (Table 1). Residue Thr396 formed a single hydrogen bond with the polar phenolic group of **L5**; amino acid Pro325 participated in two pi-alkyl interactions with two benzene rings of **L5**. Residues Pro697 and Phe398 were involved in pi-alkyl and pi-sigma interactions with two benzene rings of **L5**, respectively (Figures 2 and S1). Open chain analog **L6** of *para*-sulfonato-calix[4]arenes generated five physical interactions with the RdRp enzyme,

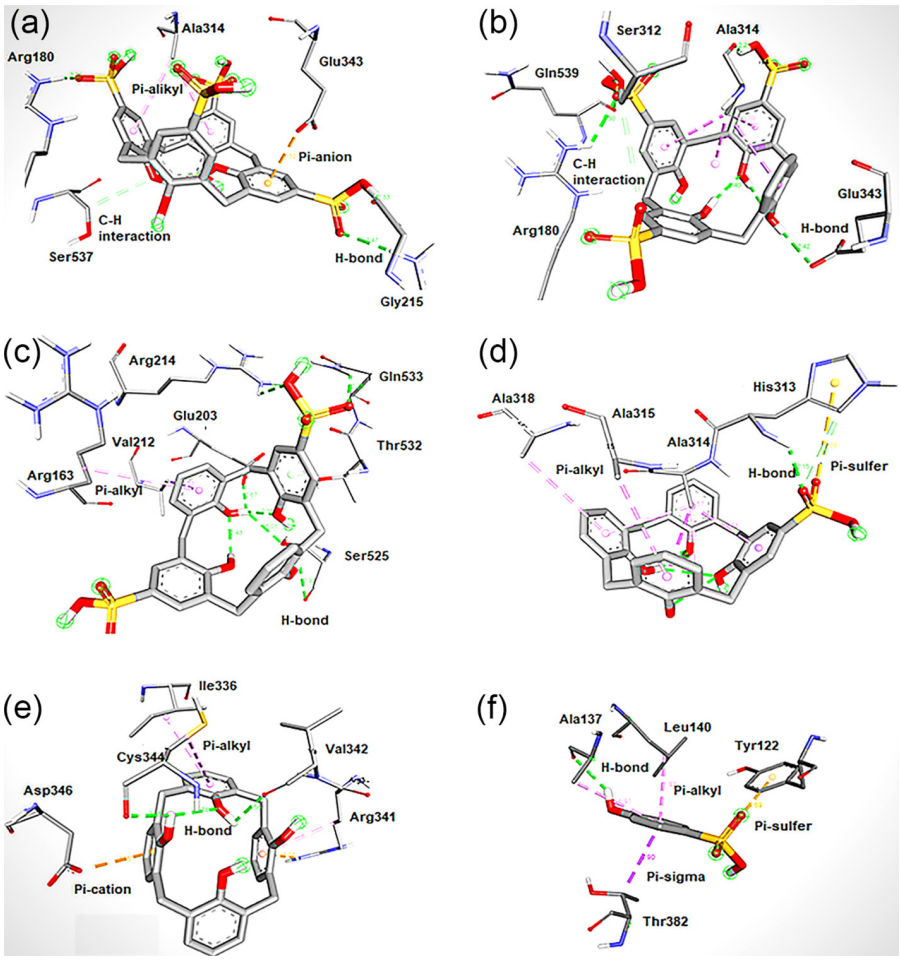

Figure 2. 3D interactions of (a) **L1**-RdRp complex, (b) **L2**-RdRp complex, (c) **L3**-RdRp complex, (d) **L4**- RdRp complex, (e) **L5**-RdRp complex and (f) **L6**-RdRp complex.

resulting in the binding energy of –5.3 kcal mol^{-1} (Table 1). Each of the residues Ser684, Arg626, Tyr658, and Thr682 developed a single hydrogen bond with three oxygen atoms and one polar hydrogen atom of the sulfonate group of **L6**, respectively (Figures 2 and S1). Further residue Asp625 of RdRp and the benzene ring of **L6** were involved in the pi-anion interaction.[38]

Docking analysis of selected compounds against helicase

Docking results indicate that **L1** formed seven physical interactions with the active sites of helicase, resulting in a binding energy of –10.1 kcal mol^{-1} (Table 2). Each of the residues Arg180, Arg163, and Gly215 formed a single hydrogen bond with two sulfonate groups of **L1**. Amino acid Ala314 formed two pi-alkyl interactions with two benzene rings of **L1**. Residues Glu343 and Ser537 participated in pi-sulfur and carbon-hydrogen interactions with the benzene ring and phenolic group of **L1**, respectively (Figures 3 and S2, SI section). Similarly, eight non-covalent forces were developed between **L2** and active sites of helicase generating the highest binding energy of –9.6 kcal mol^{-1} (Table 2). Each of the residues Arg180, Ala314, Gln539, and Glu343 was involved in a single hydrogen bond interaction with two sulfonate groups and one phenolic group of **L2**, respectively. One pi-sigma and three pi-alkyl interactions were developed by residue Ala314 with three benzene rings and one phenolic group of **L2** (Figures 3 and S2). Compound **L3** formed eight physical interactions with the active sites of the helicase enzyme of SARS-CoV-2; these non-covalent forces resulted in the binding energy of –9.4 kcal mol^{-1} (Table 2). Residue Ser525 established two hydrogen bond interactions with two phenolic groups at the lower rim of **L3**, similarly, each of the residues Glu203, Gln533, and Glu302 was involved in a single conventional hydrogen bond interaction with either sulfonate or phenolic group of **L3**. Further, the residues Arg163, Val212, and Thr532 established pi-alkyl, pi-sigma, and carbon-hydrogen interactions, respectively, with two benzene rings of **L3** (Figures 3 and S2). Compound **L4** was involved in

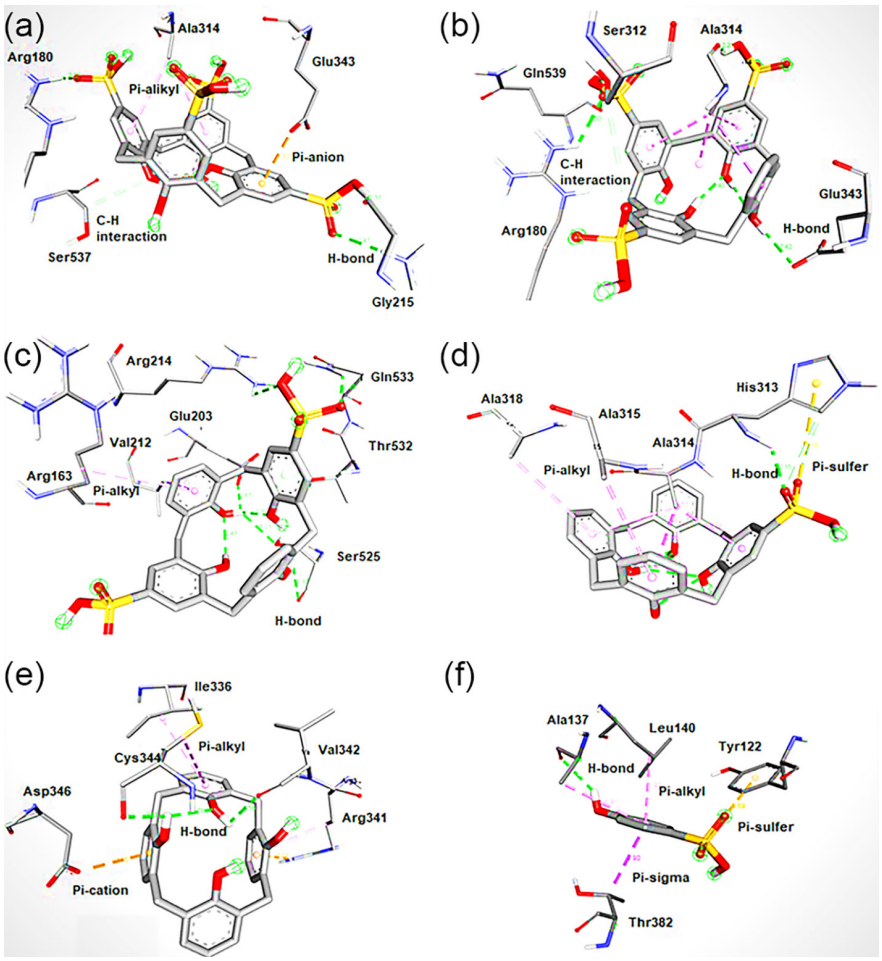

Figure 3. 3D interactions of (a) **L1**-helicase complex, (b) **L2**-helicase complex, (c) **L3**-helicase complex, (d) **L4**-helicase complex, (e) **L5**-helicase complex and (f) **L6**-helicase complex.

eight non-covalent forces with the active sites of helicase resulting in a binding energy of –8.9 kcal mol^{-1} (Table 2). Interestingly, residue Ala314 formed three pi-sigma interactions with three different benzene rings of **L4**; the residue was also involved in a pi-alkyl interaction with another benzene ring of **L4**. Amino acid His313 formed one conventional hydrogen bond interaction and one pi-sulfur interaction with the same sulfonate group of **L4**.[39] The residues Ala315 and Ala318 formed pi-alkyl interactions separately with two benzene rings of **L4** (Figures 3 and S2).

Similarly, compound **L5** established six physical interactions with the active sites of RdRp; these forces resulted in a binding energy of –5.89 kcal mol^{-1} (Table 2). Each of the residues Cys344 and Val342 formed a single conventional hydrogen bond interaction with two separate phenolic groups of **L5**. Each of the residues Cys344 and Ile336 formed a single pi-alkyl interaction with the same benzene ring of **L5**. Amino acids Arg341 and Asp346 generated pi-anion and pi-cation interactions, respectively with two separate benzene rings of **L5** (Figures 3 and S2). In case of helicase, the open chain analog **L6** formed five non-covalent interactions to its active pocket; these interactions resulted in a binding energy of –5.12 kcal mol^{-1} (Table 2). The residue Ala137 formed hydrogen bonding

Table 2. Binding affinity, number of interactions, nature of interactions, distance of interactions, and interacting residues of selected compounds (**L1-L6**) against helicase

Compound	Binding energy / (kcal mol^{-1})	Number of interactions	Nature of interactions	Interaction distance / Å	Interacting residue
L1	–10.1	7	Pi-sulfur	2.33	Glu343
			H-bond	2.47	Gly215
			H-bond	2.29	Arg163
			H-bond	3.43	Arg180
			Pi-alkyl	4.50	Ala314
			Pi-alkyl	4.51	Ala314
			Carbon-H	3.68	Ser537
L2	–9.6	8	Pi-sigma	4.09	Ala314
			Pi-alkyl	3.92	Ala314
			Pi-alkyl	4.21	Ala314
			Pi-alkyl	3.49	Ala314
			H-bond	1.50	Ala314
			H-bond	2.40	Arg180
			H-bond	2.42	Gln539
			H-bond	3.04	Glu343
L3	–9.4	8	Pi-sigma	3.51	Val212
			Pi-alkyl	3.79	Arg163
			H-bond	2.67	Glu203
			H-bond	3.01	Arg214
			Carbon-H	4.92	Thr532
			H-bond	2.35	Ser525
			H-bond	2.99	Ser525
			H-bond	1.97	Gln533
L4	–8.9	8	H-bond	2.15	His313
			Pi-alkyl	3.57	Ala314
			Pi-sigma	5.02	Ala314
			Pi-sigma	3.73	Ala314
			Pi-sigma	3.47	Ala314
			Pi-alkyl	3.05	Ala315
			Pi-alkyl	4.60	Ala318
			Pi-sulfur	5.38	His313
L5	–5.89	6	H-bond	2.56	Val342
			Pi-alkyl	4.54	Cys344
			Pi-alkyl	4.77	Ile336
			Pi-anion	3.79	Arg341
			Pi-cation	3.49	Asp346
			H-bond	3.34	Cys344
L6	–5.12	5	Pi-sulfur	5.96	Tyr122
			Pi-sigma	3.21	Thr382
			Pi-alkyl	4.92	Leu140
			Pi-alkyl	4.91	Ala137
			H-bond	2.53	Ala137

and pi-alkyl interactions with the benzene ring and phenolic group of **L6** respectively. Residues Tyr122, Thr382, and Leu140 established pi-sulfur, pi-sigma, and pi-alkyl interactions respectively with the same benzene ring of **L6** (Figures 3 and S2).

To investigate further the efficacy of compounds (**L1-L6**), a few commercially available antiviral drugs such as oseltamivir, favipiravir, chloroquine, hydroxychloroquine, ribavirin, and remdesivir were docked against the RdRp and helicase proteins using the same docking protocol. Docking results are given in Table 3. The 2D and 3D interactions of six antiviral drugs against RdRp and helicase enzymes of SARS-CoV-2 are provided in the SI section (Figures S3, S4, and S5).

Table 3. The binding affinities of selected compounds (**L1-L6**) and six currently used drugs for SARS-CoV-2 as obtained from a molecular docking study

Compound	Binding energy / (kcal mol^{-1})	
	RdRp	Helicase
L1	−8.9	−10.1
L2	−8.7	−9.6
L3	−8.5	−9.4
L4	−8.1	−8.9
L5	−6.2	−5.8
L6	−5.3	−5.1
Chloroquine	−7.3	−6.1
Favipiravir	−6.3	−5.5
Hydroxychloroquine	−6.4	−5.8
Oseltamivir	−6.3	−5.2
Ribavirin	−5.8	−5.4
Remdesivir	−8.9	−8.5

RdRp: nsp12 RNA-dependent RNA polymerase.

Molecular dynamic simulation study

Among all ligands, **L1** formed stable complexes with RdRp (7C2K) and helicase (6ZSL) of SARS-CoV-2 therefore, their apoproteins and protein-ligand complexes were subjected to 100 ns simulation to analyze various parameters, such as RMSD, RMSF, Rg, number of hydrogen bonds, SASA, PCA, and Mm/BPSA for the confirmation and validation of stability of respective protein-ligand complexes.

Root mean square deviation

Backbone RMSD was calculated for apoproteins (7C2K and 6ZSL) and protein-ligand complexes (7C2K-L1 and 6ZSL-L1) to predict the structural and conformational stability of the viral proteins and their complexes. Figures 4a and 4b show the backbone RMSD data of apoproteins and protein-compounds complexes. The average RMSD values of 7C2K, 7C2K-L1, 6ZSL, and 6ZSL-L1 were documented as 0.35 ± 0.019, 0.49 ± 0.019, 0.45 ± 0.039 and 0.39 ± 0.030 nm, respectively (Figures 4a and 4b). After the 10 ns, the 7C2K-L1 complex system gained equilibrium and

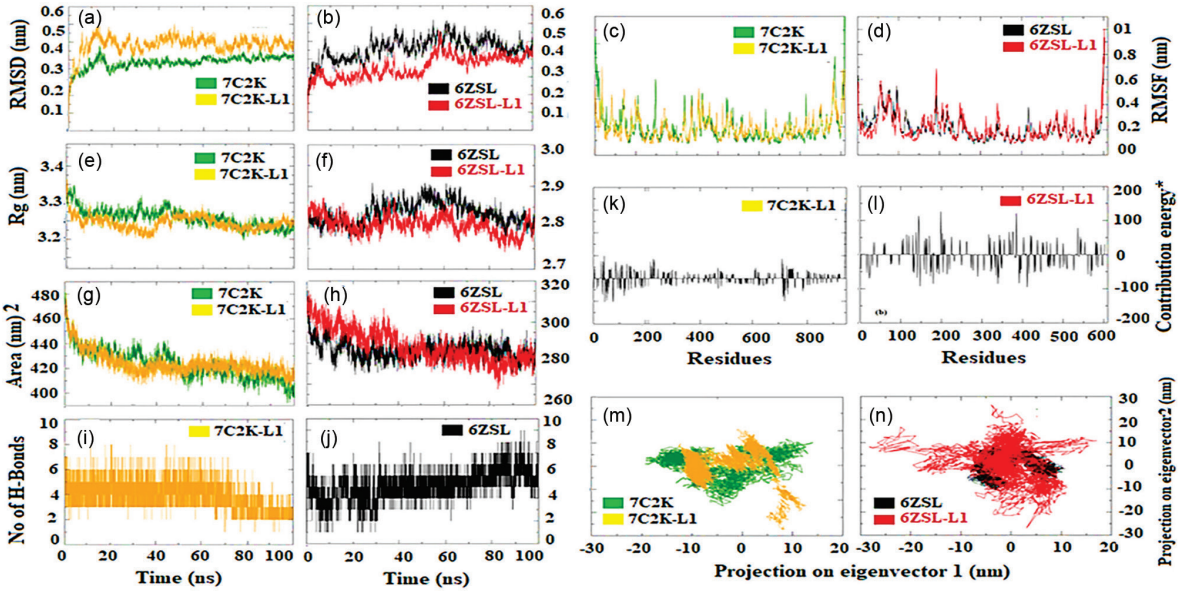

Figure 4. Root mean square deviation plot of (a) 7C2K and 7C2K-**L1** (b) 6ZSL and 6ZSL-**L1**; root mean square fluctuations plot of (c) 7C2K and 7C2K-**L1** (d) 6ZSL and 6ZSL-**L1**; the radius of gyration plot of (e) 7C2K and 7C2K-**L1** (f) 6ZSL and 6ZSL-**L1**; solvent accessible surface area (SASA) plot of (g) 7C2K and 7C2K-**L1** (h) 6ZSL and 6ZSL-**L1**; the number of H-bonds plot of (i) 7C2K-**L1** (j) 6ZSL-**L1**; the plot of contribution energy (kcal mol^{-1}) *vs*. residue number for (k) 7C2K-**L5** (l) 6ZSL-L1; principal component analysis (PCA) of (m) 7C2K and 7C2K-**L1** (N) 6ZSL and 6ZSL-**L1**. Contribution energy is taken in kcal mol^{-1}. Green, yellow, black, and red colors represent 7C2K, 7C2K-**L1**, 6ZSL, and 6ZSL-**L1** systems, respectively.

displayed less fluctuation for the rest of the simulation time inferring that **L1** was not dissociated from 7C2K and stably bound in its complementary location within the active pocket of 7C2K. Similarly, the 6ZSL-**L1** complex system remained in equilibrium from the beginning up to 58 ns; however, a sudden increase in the RMSD value was recorded at 60 ns, which could be attributed to the flexibility of the capping loop (Figures 4a and 4b). After 60 ns, the 6ZSL-**L1** complex system reached equilibrium and maintained stability until the end of the simulation.[40]

Root mean square fluctuation

The fluctuation of each residue was calculated in terms of RMSF to gain a better insight into the regions of proteins that fluctuate upon binding during the simulation. In other words, the RMSF value predicts the conformational changes occurring at the residue level within a protein macromolecule induced by ligand binding. The RMSF plots of the Cα atoms of the 7C2K, 7C2K-**L1**, 6ZSL, and 6ZSl-**L1** are given in Figures 4c and 4d. The average RMSF values of 0.20 ± 0.090, 0.20 ± 0.085, 0.2 ± 0.088, and 0.20 ± 0.075 nm were recorded for 7C2K, 7C2K-**L1**, 6ZSL, and 6ZSL-**L1**, respectively. Additionally, it was observed that both complexes (7C2K-**L1** and 6ZSL-**L1**) and compound **L1** exhibited similar fluctuations during the simulation, suggesting the stability of both complex systems (Figures 4c and 4d).[41]

Radius of gyration

The distribution of all atoms of a protein molecule around its axis, known as the center of gravity, is measured by the radius of gyration. Compactness and conformational variations of the apoproteins (7C2K and 6ZSL) and protein-compound complexes (7C2K-**L1** and 6ZSL-**L1**) were predicted using a 100 ns molecular dynamics trajectory (Figures 4e and 4f). The average Rg values for 72CK, 7C2K-**L1**, 6ZSL, and 6ZSL-**L1** were calculated as 3.250 ± 0.002, 3.257 ± 0.005, 2.850 ± 0.050 and 2.800 ± 0.050 nm, respectively (Figures 4e and 4f). It was also observed that the Rg values of the two protein-ligand complexes decreased during the simulation, indicating that the protein structure gained stability and compactness upon binding to ligand molecules.[42]

Solvent accessible surface area

SASA was utilized to assess the interaction and exposure of the protein-ligand complex to the solvent throughout the simulation. Consequently, the SASA of the complexes was calculated to gauge the extent of conformational changes occurring during the interaction. SASA values are affected by the hydrophobic residues that become exposed to the solvent environment upon binding with the inhibitor molecules. The analyzed average SASA values of 428.976 ± 2.501, 430.146 ± 1.556, 290.577 ± 2.453, and 293.011 ± 1.109 nm^2 were recorded for the 7C2K, 7C2K-**L1**, 6ZSL, and 6ZSl-**L1**, respectively (Figures 4g and 4h). Interestingly, the surface area of both the proteins and their complexes decreased, with relatively lower SASA values than the starting period.[43] Approximately 40 and 30 nm^2 of surface area were altered during the simulation for 7C2K-**L1** and 6ZSL-**L1**, respectively.

Principal component analysis

During the 100 ns simulation time, PCA was employed to identify important motions in the apoproteins and protein-compound complexes. It is widely acknowledged that the first few eigenvectors best describe the overall motions of proteins. According to the overall PCA result, the 7C2K-**L1** complex is deemed more stable than the 6ZSL-**L1** complex, as it does not exhibit higher correlated motions. A 2D projection plot from the first two eigenvectors was generated to offer superior visual representations of the data (Figures 4m and 4n). The motions of the protein in phase space are well described by the 2D projection plot.[44]

Hydrogen bonds analysis

The strength and stability of the ligand's binding to the protein are evaluated by counting the number of hydrogen bonds formed between the protein and ligand. A reasonable number of hydrogen bonds were observed for both the 7C2K-**L1** (yellow) and 6ZSL-**L1** (black) complex systems (Figures 4i and 4j). The maximum number of 8 and 10 hydrogen bonds were documented for 7C2K-**L1** and 6ZSL-**L1**, respectively. Additionally, fluctuations were noted in several hydrogen bonds throughout the simulation for both the 7C2K-**L1** and 6ZSL-**L1** complex systems, suggesting that the binding site of the compounds underwent conformational modifications.[45]

MM/PBSA binding free energy analysis

Using the MM/PBSA approach, the binding free energy of the protein-compound complex was computed during the final 20 ns of the MD production run, with calculations performed at intervals of 100 ps from the MD trajectories. The production run was conducted for all intervals at a temperature of 300 K and a pressure of 1 atm.

MmPbSaStat.py script was used to calculate the average free binding energy as well as its standard deviation/error from the g_mmpbsa output files. The inhibitor **L1** showed binding free energy of −592 and −1040 kJ mol^{-1} with the 7C2K and 6ZSL proteins, respectively, indicating that both complex systems remained stable throughout the simulation time. Additionally, the contribution of each protein residue to the interaction with the inhibitor **L1** was determined in terms of binding free energy. This was achieved by decomposing the total binding free energy of the system into *per*-residue contribution energy. The contribution of each residue's energy provides valuable insight into the "crucial" residues that facilitate the binding of the **L1** molecule to the protein.[46,47] It was found that Arg35, Lys43, Lys52, Lys75, Arg76, Arg118, Lys716, Lys720, Arg723, and Arg735 residues of the 7C2K protein contributed higher than −70 KJ mol^{-1} binding energy and thereby are hotspot residues in binding with the inhibitor **L1** (Figure 4k). While 6ZSL protein residues Arg17, Arg23, Arg24, Asp115, Asp121, Lys133, Lys141, Lys148, Arg163, Lys173, Arg175, Arg180, Arg188, Lys194, Lys204, Arg214, Lys290, Lys322, Arg334, Arg339, Arg341, Arg392, Arg394, Arg411, Lys416, Arg429, Arg445, Arg562 and Arg569 contributed greater than −50 KJ mol^{-1} binding energy and thereby are hotspot residues in binding with the inhibitor **L1** (Figure 4l).

Pharmacological and toxicological analyses

Determining the pharmacokinetics, drug-likeness, toxicity, physicochemical, and pharmacological properties of a compound are preliminary steps in the drug discovery process. These parameters can predict the druggability of a compound. In this context, various properties such as lipophilicity, water solubility, adherence to Lipinski's rules, number of rotatable bonds, blood-brain barrier permeation, and toxicological properties of selected compounds (**L1-L6**) were predicted using an *in silico* model. Details are given in Table 4.

Discussion

The inhibitory potency of inhibitors (**L1-L6**) was investigated against both the RdRp and helicase enzymes of SARS-CoV-2 using docking techniques. The results indicate that all inhibitors (**L1-L6**) demonstrate inhibitory efficacy against both RdRp and helicase enzymes by forming strong interactions with their respective active sites. This leads to the formation of stable protein-ligand complexes. The inhibitors (**L1-L6**) exhibit the following order of inhibitory potency for both RdRp and helicase enzymes based on binding affinity: **L1 > L2 > L3 > L4 > L5 > L6**. The inhibitors (**L1-L4**) are ranked according to the number of sulfonate groups at the upper rim of *para*-sulfonato-calix[4]arenes as follows: **L1 > L2 > L3 > L4**. It is evident from docking data that the inhibitory potency of inhibitors (**L1-L6**) considerably increases as the number of sulfonate groups increases. Compound **L1**, with four sulfonate groups at the upper rim, exhibits the highest binding affinity, as indicated in Tables 1 and 2, resulting in stable **L1**-protein complexes. Compound **L1** is firmly bound in its complementary location within the active

Table 4. *In silico* ADME and toxicity prediction of selected compounds (**L1-L6**)

Property	L1	L2	L3	L4	L5	L6
Hepatotoxicity	inactive	inactive	inactive	inactive	inactive	inactive
Carcinogenicity	inactive	inactive	inactive	inactive	inactive	inactive
Immunotoxicity	inactive	inactive	inactive	inactive	inactive	inactive
Mutagenicity	inactive	inactive	inactive	inactive	inactive	inactive
Cytotoxicity	inactive	inactive	inactive	inactive	inactive	inactive
Ecotoxicity	inactive	inactive	inactive	inactive	inactive	inactive
Clinical toxicity	inactive	inactive	inactive	inactive	inactive	inactive
Predicted LD_{50} / (mg kg^{-1})	3530	3530	3530	3530	4880	1800
Predicted toxicity class	5	5	5	5	5	4
Log $P_{w/o}$	1.61	2.15	2.01	3.64	5.30	0.07
Log S	−5.36 (MS)	−5.75 (MS)	−6.15 (PS)	−6.55 (PS)	−6.97 (PS)	−0.10 (PS)
No. of rotatable bonds	04	03	02	01	00	01
Lipinski'srules	03	03	02	01	00	00
BBB permeation	no	no	no	no	no	no
GI absorption	low	low	low	low	high	high

MS: moderately soluble; PS: poorly soluble; Log S: water solubility; Log $P_{w/o}$: lipophilicity: consensus; BBB: blood-brain barrier; GI: gastrointestinal; LD_{50}: median lethal dose 50.

pocket of both proteins, forming hydrogen bonds between the sulfonate groups of **L1** and catalytic residues of both RdRp and helicase enzymes (Figures 2 and 3). Complex formation is governed by pi-anion, pi-alkyl, pi-sulfur, and carbon-hydrogen interactions. As the number of sulfonate groups in compounds **L2**, **L3**, and **L4** gradually decreases (Tables 1 and 2), their inhibitory potency correspondingly declines. To further elaborate on the role of the sulfonate group, compound **L5**, lacking the sulfonate group, was docked against the target proteins. It exhibited very low binding affinity compared to the inhibitors (**L1-L4**), (Tables 1 and 2). This confirms the crucial role of the sulfonate group in complex formation. From the aforementioned facts, it is established that the number of sulfonate groups at the upper rim of *para*-sulfonato-calix[4] arenes plays a vital role in the formation of a stable protein-inhibitor complex. To further understand the role of the intrinsic cyclic core of *para*-sulfonato-calix[4]arenes in the formation of protein-ligand complexes, the open chain analogue **L6** of *para*-sulfonato-calix[4]arenes was docked against both RdRp and helicase enzymes of SARS-CoV-2. In both cases, **L6** exhibits weak interactions and low binding affinity compared to inhibitors (**L1-L5**), as indicated in Tables 1 and 2. This confirms that the intrinsic cyclic core of *para*-sulfonato-calix[4]arenes enhances the binding ability of inhibitors (**L1-L5**) by securely locking them into their complementary locations within the active pocket of both RdRp and helicase enzymes. Consequently, it is concluded that both the number of sulfonate groups and the intrinsic cyclic core of *para*-sulfonato-calix[4] arenes amplify the inhibitory potency of inhibitors by facilitating strong physical interactions between the sulfonate groups of inhibitors and the catalytic residues of both RdRp and helicase enzymes of SARS-CoV-2. To assess the effectiveness of compounds (**L1-L6**), a docking analysis was conducted on a selection of currently used antiviral drugs, including oseltamivir, favipiravir, chloroquine, hydroxychloroquine, ribavirin, and remdesivir, against the RdRp and helicase proteins. The same docking protocol used for the other ligands (**L1-L6**) was followed for this analysis. The results indicate that inhibitors (**L1-L6**) generally exhibit higher binding affinity against both proteins compared to the binding affinity of commonly used drugs (Table 3). However, it is noteworthy that remdesivir displays binding energy equal to **L1** and greater than **L2-L6** against RdRp. This suggests that **L1** and remdesivir have comparable affinity toward RdRp. Additionally, it has been observed that compounds (**L1-L6**) demonstrate a higher binding affinity for helicase compared to RdRp. This phenomenon could be attributed to the conformational flexibility of inhibitors within the active pocket of the helicase protein. Among all compounds, **L1** exhibits the highest binding affinity for both proteins, RdRp, and helicase. Therefore, its protein-ligand complexes (7C2K-**L1** and 6ZSL-**L1**), along with the apoproteins (7C2K and 6ZSL), were subjected to a 100 ns molecular dynamics simulation to validate the formation of stable protein-ligand complexes. RMSD is used to assess the structural and conformational stability of both the apoproteins and the protein-ligand complexes. The deviations shown by RMSD values for both complex systems (7C2K-**L1** and 6ZSL-**L1**) were recorded as 0.49 and 0.39 nm, respectively (Figures 4a and 4b). These results are consistent with the deviations in RMSD values for the RdRp-ATP, RdRp-galidesivir, and RdRp-remdesivir complex systems, which were documented as 0.43, 0.37, and 0.46 nm, respectively.[48] RMSD values suggest that both complexes are stable during the simulation time, indicating that **L1** is stably bound in its complementary conformation located in the active pocket of both proteins. RMSF is employed to predict the conformational changes that occur at the residue level in a protein induced by ligand binding. The results indicate that the majority of the protein residues are stabilized within an acceptable range of RMSF values of 0.6 nm, suggesting that residues of both proteins, upon binding with **L1**, exhibit fewer fluctuations and greater stability. The radius of gyration is indeed a crucial tool for predicting the structural activity or compactness of proteins, as well as understanding the binding pattern of ligands and proteins. A lower Rg value indeed signifies higher compactness and greater stability, while a higher Rg value indicates the opposite. The fact that Rg values remain lower for both complexes throughout the simulation suggests that protein structures gain both stability and compactness upon binding to **L1**. Relative SASA is employed to anticipate the conformational changes occurring in both proteins upon binding.[49] It is evident from Figures 4g and 4h that the surface area changed during the simulation for both the 7C2K-**L1** and 6ZSL-**L1** complexes, indicating conformational changes in both the RdRp and helicase proteins upon binding of **L1**. The SASA results confirm the binding of **L1** to the active pocket of both proteins. PCA is then applied to identify the crucial motions in both the apoprotein and protein-ligand complexes. The PCA results indicate that the 7C2K-**L1** complex is more stable than the 6ZSL-**L1** complex, as it does not exhibit higher correlated motions. Further, the PCA results align with the findings from Rg, suggesting that the binding of **L1** to the active site of both proteins mitigates major dynamic behaviors of the target proteins. To assess the strength and stability of the ligand's binding to the protein, the number of hydrogen bonds generated between the protein and **L1**

is counted. The results of the hydrogen bond analysis suggest that **L1** forms stable complexes with the pathogenic proteins 7C2K and 6ZSL, and also indicate that both complexes remain stable throughout the simulation period. Generating a PBSA energy model is an appropriate and essential technique in molecular mechanics (MM) for calculating the binding energy of selected protein-ligand complexes. The binding energy offers valuable insights into the stability of the protein-ligand complex by indicating the consistency of non-bonded interactions throughout the simulation. The results indicate that compound **L1** exhibits strong binding energy with both target proteins, confirming the robust binding of **L1** to the catalytic residues of both proteins. The calculations of binding free energy *per* residue further confirm that the catalytic residues of both proteins are strongly and firmly involved in complex formation with the inhibitor **L1**. The MD simulation results conclude that **L1** forms stable complexes with both the proteins RdRp and helicase. Additionally, the druggability investigation of selected compounds (**L1-L6**) predicts that all compounds display drug-likeness properties. The lipophilicity (Log $P_{w/o}$) for compounds **L1** and **L2** were noted as 1.61 and 2.15, respectively (Table 4), which are superior to the commercially available antiviral drugs favipiravir (–0.27) and remdesivir (1.53). This suggests that both inhibitors **L1** and **L2** possess the ability to penetrate both human cells and viral membranes. Furthermore, the result of gastrointestinal (GI) absorption for **L1** is also consistent with the result of the antiviral drug favipiravir.[50] Each of the compounds **L1** and **L2** also exhibits three violations when applying Lipinski's rules. It is worth noting that many medicines that are widely used as effective pharmaceuticals are reported to have three violations.[51] The toxicity results provided in Table 4 indicate that interestingly, all selected compounds were found to be inactive against carcinogenicity, immunotoxicity, mutagenicity, cytotoxicity, ecotoxicity, and clinical toxicity. The median lethal dose weight (LD_{50}) was predicted to vary from 3530 to 4880 mg kg^{-1} for all compounds, categorizing them as class 5 toxic, except for **L6**, for which LD_{50} was noted as 1800 mg kg^{-1}, grading it as class 4 toxic.[36] The toxicity findings suggest that all these compounds are non-carcinogenic and non-toxic in nature. Due to their favorable membrane permeability, aqueous solubility, molecular flexibility, non-toxicity, and absence of blood-brain barrier penetration, molecules **L1** and **L2** are anticipated to be utilized as lead candidates. Considering the docking score, druggability, non-toxicity, and MD simulation results, **L1**, along with other inhibitors, may be utilized to target COVID-19 infection by inhibiting viral replication and repair processes.

Conclusions

Molecular docking and molecular dynamic simulations were employed as useful tools to evaluate the inhibitory potency of *para*-sulfonato-calix[4]arenes against SARS-CoV-2, which is affecting people worldwide. The docking results indicate that *para*-sulfonato-calix[4]arenes efficiently bind to the active sites of RdRp and helicase, suggesting that these compounds can efficiently suppress viral replication. Among all screened inhibitors, **L1** demonstrates strong performance for RdRp and helicase with more negative binding energies of –8.9 and –10.1 kcal mol^{-1}, respectively. MD simulation results confirm the stability of the 7C2K-**L1** and 6ZSL-**L1** complexes. *para*-Sulfonato-calix[4]arenes molecules are also found to be more efficacious than commonly used antiviral drugs. Furthermore, it appears that *para*-sulfonato-calix[4]arenes have a higher binding potential against helicase than RdRp. Docking results also display that the intrinsic core cyclic structure of *para*-sulfonato-calix[4]arenes, the number of sulfonate groups at the upper rim of *para*-sulfonato-calix[4]arenes, and the conformational flexibility of the inhibitor in the active pocket are the main factors that significantly influence inhibitor binding to proteins. Toxicity and druggability data also suggest that compounds **L1** and **L2** may be utilized as lead candidates for the inhibition of RdRp and helicase. This investigation suggests that *para*-sulfonato-calix[4]arenes may be utilized as potential inhibitors against SARS-CoV-2. For further confirmation and validation, *in vitro* and *in vivo* studies are recommended.

Supplementary Information

Supplementary information is available free of charge at http://jbcs.sbq.org.br as a PDF file.

Acknowledgments

The authors extend their appreciation to the researchers supporting Project number (RSP2024R45) at King Saud University, Riyadh, Saudi Arabia, for financial support.

Author Contributions

Khalid Khan was responsible for conceptualization, data curation, and project administration; Habib Rahman for writing the original draft and visualization; Tanzeel Shah for validation and formal analysis; Haroon ur Rashid for writing-review and editing and software; Nasir Ahmad for validation, data curation and software; Akhtar Muhammad for visualization, resources, and formal analysis; Muhammad Naveed

Umar for data curation and formal analysis; Naila Gulfam for investigation and writing-review and editing; Muhammad Zahoor for visualization, validation, and formal analysis; Riaz Ullah for funding acquisition, resources, and visualization; Essam A. Ali for data curation, investigation, and funding acquisition.

References

1. Wu, A.; Peng, Y.; Huang, B.; Ding, X.; Wang, X.; Niu, P.; Meng, J.; Zhu, Z.; Zhang, Z.; Wang, J.; Sheng, J.; Quan, L.; Xia, Z.; Tan, W.; Cheng, G.; Jiang, T.; *Cell Host Microbe* **2020**, *27*, 325. [Crossref]
2. Velavan, T. P.; Meyer, C. G.; *Trop. Med. Int. Health* **2020**, *25*, 278. [Crossref]
3. Wilder-Smith, A.; Osman, S.; *J. Travel Med*. **2020**, *27*, taaa227. [Crossref]
4. Jee ,Y.; *Epidemiol. Health* **2020**, *42*, e2020013. [Crossref]
5. WHO COVID-19 dashboard, https://data.who.int/dashboards/covid19/cases, accessed in June 2024.
6. Li, F.; *Annu. Rev. Virol*. **2016**, *3*, 237. [Crossref]
7. Wu, C.; Chen, X.; Cai, Y.; Zhou, X.; Xu. S.; Huang, H.; Zhang, L.; Zhou, X.; Du, C.; Zhang, Y.; Song, J.; Wang, S.; Chao, Y.; Yang, Z.; Xu, J.; Zhou. X.; Chen, D.; Xiong, W.; Xu, L.; Zhou, F.; Jiang, J.; Bai, C.; Zheng, J.; Song, Y.; *JAMA Intern. Med*. **2020**, *180*, 934. [Crossref]
8. Tang, Q.; Song, Y.; Shi, M.; Cheng, Y.; Zhang, W.; Xia, X. Q.; *Sci. Rep*. **2015**, *26*, 17155. [Crossref]
9. Yan, W.; Zheng, Y.; Zeng, X.; He, B.; Cheng, W.; *Signal Transduction Targeted Ther.* **2022**, *7*, 26. [Crossref]
10. Caruthers, J. M.; McKay, D. B.; *Curr. Opin. Struct. Biol*. **2002**, *12*, 123. [Crossref]
11. Liu, C.; Zhou, Q.; Li, Y.; Garner, L. V.; Watkins, S. P.; Carter, L. J.; Smoot, J.; Gregg, A. C.; Daniels, A. D.; Jervey, S.; Albaiu, D.; *ACS Cent. Sci*. **2020**, *6*, 315. [Crossref]
12. Cáceres, O. I. A.; Timóteo, F.; Santos, K. F. D. P.; Vasconcelos, R. R. P.; Martines, M. A. U.; Jorge, J.; Rashid, H. U.; *Orbital: Electron. J. Chem*. **2021**, *13*, 350. [Crossref]
13. Mei, M.; Tan, X.; *Front. Mol. Biosci.* **2021**, *8*, 671263. [Crossref]
14. Khan, T.; Khan, M. A.; Mashwani, Z. U.; Ullah, N.; Nadhman, A.; *Biocatal. Agric. Biotechnol*. **2021**, *31*, 101890. [Crossref]
15. Rehman, M. F.; Akhter, S.; Batool, A. I.; Selamoglu, Z.; Sevindik, M.; Eman, R.; Mustaqeem, M.; Akram, M. S.; Kanwal, F.; Lu, C.; Aslam, M.; *Antibiotics* **2021**, *10*, 1011. [Crossref]
16. Noruzi, E. B.; Molaparast, M.; Zarei, M.; Shaabani, B.; Kariminezhad, Z.; Ebadi, B.; Shafiei-Irannejad, V.; Rahimi, M.; Pietrasik, J.; *Eur. J. Med. Chem*. **2020**, *190*, 112121. [Crossref]
17. Perret, F.; Lazar, A. N.; Coleman, A. W.; *Chem. Commun*. **2006**, *23*, 2425. [Crossref]
18. Geller, C.; Fontanay, S.; Mourer, M.; Dibama, H. M.; Regnouf-de-Vains, J. B.; Finance, C.; Duval, R. E.; *Antiviral Res*. **2010**, *88*, 343. [Crossref]
19. RCSB Protein Data bank, https://www.rcsb.org, accessed in June 2024.
20. *BIOVIA Discovery Studio Visualizer*; BIOVIA Dassault Systems; San Diego, USA, 2020.
21. *PyRx Virtual Screening Tool*, v. 0.9.7; Sarkis Dallakyan, USA, 2015.
22. Morris, G. M.; Lim-Wilby, M.; *Methods Mol. Biol.* **2008**, *443*, 365. [Crossref]
23. Evans, D. A.; Evans, S.; Rubenstein, S.; *ChemDraw*, v20.0; PerkinElmer Inc., Waltham, MA, USA, 2021; Evans, D. A.; *Angew. Chem., Int. Ed*. **2014**, *53*, 11140. [Crossref]
24. O'Boyle, N. M.; Banck, M.; James, C. A.; Morley, C.; Vandermeersch, T.; Hutchison, G. R.; *J. Cheminf.* **2011**, *3*, 1758. [PubMed]
25. *AutoDock Vina*, v. 1.2.0; Molecular Graphics Lab, The Scripps Research Institute, USA, 2009; Trott, O.; Olson, A. J.; *J. Comput. Chem.* **2009**, *31*, 455 [Crossref]
26. Dallakyan, S.; Olson, A. J. In *Chemical Biology*; Hempel, J. E.; Williams, C. H.; Hong, C. C., eds.; Humana Press: New York, USA, 2015, p. 243-250.
27. Jejurikar, B. L.; Rohane, S. H.; *Asian J. Res. Chem.* **2021**, *14*, 135. [Crossref] [Link] accessed in June 2024
28. Torvalds, L.; *Linux 5.4* package; University of Helsinki, Finland, 1991.
29. Spoel, D. V. D.; Lindahl, E.; Hess, B.; Groenhof, G.; Mark, A. F.; Berendsen, H. J. C.; *GROMACS*; University of Groningen Royal Institute of Technology, Stockholm, Sweden, 1991; Spoel, D. V. D.; Lindahl, E.; Hess, B.; Groenhof, G.; Mark, A. E.; Berendsen, H. J.; *J. Comput. Chem.* **2005**, *26*, 1701. [Crossref]
30. CHARMM General Force Field (CGenFF) program, https://cgenff.silcsbio.com, accessed in June 2024.
31. Karplus, M.; *CHARMM*; Department of Chemistry, Harvard University, USA, 1983; Vanommeslaeghe, K.; Hatcher, E.; Acharya, C.; Kundu, S.; Zhong, S.; Shim, J.; Darian, E.; Guvench, O.; Lopes, P.; Vorobyov, I.; Mackerell Jr., A. D.; *J. Comput. Chem.* **2010**, *31*, 671. [Crossref]
32. Turner, P. J.; *XMGRACE*, version 5.1.19; Center for Coastal and Land-Margin Research, Oregon Graduate Institute of Science & Technology, Beaverton, OR, USA, 2005.
33. Kumari, R.; Kumar, R.; *J. Chem. Inf. Model*. **2014**, *54*, 1951. [Crossref]
34. Baker, N. A.; Sept, D.; Joseph, S.; Holst, M. J.; McCammon, J. A.; *Proc. Natl. Acad. Sci*. **2001**, *98*, 10037. [Crossref]
35. Lipinski, C. A.; Lombardo, F.; Dominy, B. W.; Feeney, P. J.; *Adv. Drug Delivery Rev*. **2012**, *64*, 4. [Crossref]
36. SwissADME, www.swissadme.ch/index.php, accessed in June 2024; Daina, A.; Michielin, O.; Zoete, V.; *Sci. Rep*. **2017**, *7*, 42717. [Crossref]
37. *ProTox* 3.0 - Prediction of Toxicity of Chemicals, https://comptox.charite.de/protox3/index.php?site=home, accessed in June 2024.

38. Ahmad, N.; Rehman, A. U.; Badshah, S. L.; Ullah, A.; Mohammad, A.; Khan, K.; *J. Mol. Struct.* **2020**, *1203*, 127428. [Crossref]
39. Ahmad, N.; Badshah, S. L.; Junaid, M.; Rehman, A. U.; Muhammad, A.; Khan, K.; *J. Biomol. Struct. Dyn*. **2021**, *39*, 3004. [Crossref]
40. Al-Karmalawy, A. A.; Dahab, M. A.; Metwaly, A. M.; Elhady, S. S.; Elkaeed, E. B.; Eissa, I. H.; Darwish, K. M.; *Front. Chem*. **2021**, *9*, 661230. [Crossref]
41. Pathak, R. K.; Gupta, A.; Shukla, R.; Baunthiyal, M.; *Comput. Biol. Chem*. **2018**, *76*, 32. [Crossref]
42. Rout, J.; Swain, B. C.; Tripathy, U.; *J. Biomol. Struct. Dyn*. **2022**, *40*, 860. [Crossref]
43. Nguyen, H. L.; Thai, N. Q.; Truong, D. T.; Li, M. S.; *J. Phys. Chem. B* **2020**, *124*, 11337. [Crossref]
44. Srivastava, M.; Mittal, L.; Kumari, A.; Asthana, S.; *Front. Mol. Biosci.* **2021**, 8, 639614. [Crossref]
45. Wakchaure, P. D.; Ghosh, S.; Ganguly, B.; *J. Phys. Chem. B* **2020**, *124*, 10641. [Crossref]
46. Shah, M.; Rahman, H.; Khan, A.; Bibi, S.; Ullah, O.; Ullah, S.; Rehman N. U.; Murad, W.; Al-Harrasi, A.; *Molecules* **2022**, *27*, 1322. [Crossref]
47. Yang, B.; Lin, S. J.; Ren, J. Y.; Liu, T.; Wang, Y. M.; Li, C. M.; Xu, W. W.; He, Y. W.; Zheng, W. H.; Zhao, J.; Yuan, X. H.; Liao, H. X.; *Int. J. Mol. Sci*. **2019**, *20*, 2568. [Crossref]
48. Mishra, A.; Rathore, A. S.; *J. Biomol. Struct. Dyn*. **2022**, *40*, 6039. [Crossref]
49. Marsh, J. A.; Teichmann, S. A.; *Structure* **2011**, *19*, 859. [Crossref]
50. Erdogan, T.; *J. Mol. Struct*. **2021**, *1242*, 130733. [Crossref]
51. Dashti, Y.; Grkovic, T.; Quinn, R. J.; *Nat. Prod. Rep.* **2014**, *31*, 990. [Crossref]

Submitted: March 22, 2024
Published online: June 25, 2024